Title

Presynaptic reorganization in the sensory hair cell after noise exposure

Abbreviated title

Presynaptic reorganization in the inner hair cell

Authors

Yan Lu[1,2,3,4], Shengxiong Wang[4], Haoyu Wang[4], Fangfang Wang[4], Hua Han[5,6,7], Jing Liu[5], Yunfeng Hua[1,2,3,4]

Affiliations

[1]Department of Otolaryngology-Head and Neck Surgery, Shanghai Ninth People's Hospital, Shanghai, China

[2]Ear Institute, Shanghai Jiao Tong University School of Medicine, Shanghai, China

[3]Shanghai Key Laboratory of Translational Medicine on Ear and Nose Diseases, Shanghai, China

[4]Shanghai Institute of Precision Medicine, Ninth People's Hospital, Shanghai Jiao Tong University School of Medicine, Shanghai, China

[5]National Laboratory of Pattern Recognition, Institute of Automation, Chinese Academy of Sciences, Beijing, China

[6]School of Artificial Intelligence, School of Future Technology, University of Chinese Academy of Sciences, Huairou District, Beijing, China

[7]CAS Center for Excellence in Brain Science and Intelligence Technology, Shanghai, China

Correspondence should be addressed to Jing Liu at liujing2016@ia.ac.cn or Yunfeng Hua at yunfeng.hua@shsmu.edu.cn

Conflicts of interest

The authors declare no competing financial interests.

Author Contributions

Y.H. designed and supervised the study; Y.L. carried out the animal experiments, Y.L., J.L., S.W. and H.W. analyzed the data; J.L. and H.H. contributed the segmentation and 3D reconstruction; F.W. assisted with the EM acquisition; Y.H., Y.L., S.W. and J.L. drafted the manuscript. All authors commented on the manuscript.

Acknowledgments

We thank Xu Ding and Bei Li for the help in the early stage of this work, thank Shanghai Jiao Tong University Instrumental Analysis Center for the assistant of XRM imaging. This work was supported by National Natural Science Foundation of China (82171133 to Y.H., 32171461 to H.H.), Industrial Support Fund of Huangpu District in Shanghai (XK2019011 to Y.H.), Innovative Research Team of High-Level Local Universities in Shanghai (SHSMU-ZLCX20211700), the Shanghai Key Laboratory of Translational Medicine on Ear and Nose Diseases (14DZ2260300), the Strategic Priority Research Program of Chinese Academy of Science (No. XDB32030208 to H.H.).

Key words

cochlear synaptopathy/ inner hair cell/ ribbon morphology/ synaptic mitochondria

Abstract

In mammals, neural encoding of sounds is mediated by ribbon-type synapses between inner ear hair cells (IHCs) and postsynaptic spiral ganglion neurons. These specialized connections are arranged along the IHC basolateral surface with gradient changes in morphology and electrophysiological properties, which are essential for the level coding of sound intensity. Large synaptic ribbons, which predominantly reside on the modiolar IHC face, are responsive to loud sounds and more susceptible to acoustic insults. Selective loss of them is the major cause for reduced cochlear audible range. However, other than fewer ribbons after noise exposure, the consequential presynaptic reorganization in the IHCs remains less characterized. Here, by means of volume electron microscopy and artificial intelligence-assisted image analysis, we investigated noise exposure-related changes in the mouse IHCs. Apart from morphological changes of the ribbon-type active zones, our quantifications reveal differential synaptic reorganization in the IHCs with staggered basolateral pole orientations as well as reduced spatial correlation between ribbons and proximal mitochondria. Together, these results argue for putative presynaptic mechanisms underlying activity-dependent structural changes in the sensory epithelial cells.

Introduction

In the mammalian cochlea, sounds are decomposed into different frequency components by the basilar membrane (BM), establishing a place-frequency map for resident sensory epithelial cells – the inner hair cells (IHCs) – as well as postsynaptic spiral ganglion neurons (SGNs) (for reviews, see (Fettiplace, 2017; Huet et al., 2019; Moser et al., 2020)). In rodents for instance, each IHC is contacted by about 20 predominantly unbranched peripheral dendrites of the type I SGNs, forming up to 25 active zones (AZs) with characteristic electron-dense and vesicle-tethering synaptic ribbons. These specialized connections are proven of an essential role for ultrafast and temporally-precise sound encoding (for reviews, see (Moser et al., 2020; Safieddine et al., 2012)). Early studies using light (Frank et al., 2010; Liberman et al., 2011; Liberman et al., 1990; Meyer et al., 2009; Wong et al., 2014) and electron microscopy (Bullen et al., 2015; Hua et al., 2021; Liberman et al., 1990; Michanski et al., 2019; Payne et al., 2021) have revealed great diversity in both pre- and postsynaptic morphology of the ribbon synapses. They are found arranging in a spatial gradient with large ribbons on the modiolar (neural) IHC face whereas small ones on the pillar (abneural) face. Such morphological heterogeneity has been proposed of functional implication, as the ribbon-bound synaptic vesicle (SV) pool increases with expanding ribbon volume (Michanski et al., 2019; Payne et al., 2021; Stamataki et al., 2006) and thus more fusion-competent SVs are made available to the synaptic release site (Joselevitch and Zenisek, 2020; Vaithianathan et al., 2016). Moreover, ribbons of different size are presumably aligned to three distinct functional and molecular SGN subtypes (Petitpre et al., 2018; Shrestha et al., 2018; Sun et al., 2018). A prevailing view on such divergent connectivity pattern of afferent connections is to enable collectively neural encoding of the entire audible range by the functionally fractionated SGNs (Heil and Peterson, 2015; Moser et al., 2020; Pangrsic et al., 2018).

89 In the mature cochlea however, these fine-structured afferent connections are
90 found most susceptive to acoustic insults and non-regenerative once lost. Even moderate
91 overexposure can lead to a permanent ribbon loss of up to ~50 % and subsequent SGN
92 death in the rodent models (Kujawa and Liberman, 2009; Liberman et al., 2015), providing a
93 plausible explanation for significant reduction in the synaptic counts observed in elder
94 mammals (Fernandez et al., 2015; Sergeyenko et al., 2013) including human (Wu et al.,
95 2019). In addition to ribbon loss (also known as cochlear synaptopathy), the IHCs appear to
96 have difficulty in maintaining a prominent ribbon gradient following noise exposure. In
97 accordance with these observations, auditory fibers with low spontaneous rates and high
98 thresholds are found more vulnerable to glutamate excitotoxicity (Furman et al., 2013),
99 inferring a selective damage on large modiolar ribbons (see review (Liberman, 2017)).
100 Therefore, coding deficits, as a causal consequence of the cochlear synaptopathy, are likely
101 implicated in the weakened auditory discrimination under background noise, which is one of
102 the hallmarks of hidden hearing loss and presbycusis (Kujawa and Liberman, 2015; Shi et al.,
103 2016).
104 Although post-exposure dynamics of the cochlear synaptopathy has been
105 extensively studied using light microscopy (LM) in different species (Fernandez et al., 2015;
106 Hickman et al., 2020; Liberman et al., 2015; Shi et al., 2016), quantitative structural
107 investigations at higher spatial resolution and with comprehensive cellular context are
108 needed for understanding the presynaptic concepts for adaptive ribbon plasticity and
109 reorganization. Most recent advances in three-dimensional (3D) electron microscopy (EM)
110 and artificial intelligence-based segmentation techniques have made it possible to volume
111 reconstruct the IHCs at unprecedent large scale and superior resolution (Bullen et al., 2015;
112 Hua et al., 2021; Liu et al., 2022; Michanski et al., 2019; Payne et al., 2021). Here, we

113 employed serial block-face scanning electron microscopy (SBEM) to capture presynaptic
114 structural changes in six large datasets of the cochlea, which were acquired from middle and
115 basal turns of juvenile mice with or without acoustic overexposure history. Specifically, we
116 quantified morphology and distribution of the ribbon-type AZs in pooled and grouped IHCs
117 following synaptopathic and non-synaptopathic exposure, as well as attempted to
118 characterize the putative ribbon-associated mitochondrial network and its synaptic activity-
119 dependent remodeling.
120

121 **Results**

122 **SBEM Imaging of Noise Exposed Cochlear Organ of Corti.** In this study, we acquired six
123 SBEM datasets of cochlea from four male CBA mice at 5-6 weeks of age (Fig 1A). The imaged
124 volumes are centered on the organs of Corti and each contains 18.7 ± 4.0 IHCs (see Table 1
125 for more dataset information). Among these are two control datasets from individual
126 animals without noise-exposure history (M1/2, taken from basal cochlear turn), whereas
127 four from the other two animals (M3/4, taken from both middle and basal turns) on the
128 post-exposure day-7 to a two-hour (2 h) pure tone of 8-16 kHz at 91-dB sound pressure level
129 (SPL). The use of this narrowband noise frequency has been previously well established and
130 yields temporary hearing loss with distinct frequency characters in an exposure dose-
131 dependent manner (Fernandez et al., 2015; Kujawa and Liberman, 2009; Liberman et al.,
132 2015). Auditory brainstem responses (ABRs) of the exposed animals confirmed transient
133 hearing threshold elevations upon the so-called synaptopathic (91-dB, 2 h) as well as non-
134 synaptopathic (85-dB, 2 h) sounds (Fig 1B and C). Specifically, the peak threshold elevation
135 of the 85-dB exposed group was at 22.6 kHz (30.00 ± 1.05 dB, n = 10) in terms of ABR test
136 frequencies on the post-exposure day one (D1), whereas the 91-dB exposed group
137 demonstrated a monotonically increased threshold elevation with the test frequency
138 starting from 8 kHz and reaching a maximum at 45.2 kHz (32.86 ± 1.38 dB, n = 7). On the
139 post-exposure day seven (D7), a full recovery in the ABR thresholds was observed in both
140 exposed groups (Fig 1B and C), suggesting the absence of a permanent hearing loss. Note
141 that there is an age-related difference in the noise susceptibility between the mature (> 8
142 weeks) and our juvenile (5-6 weeks) CBA mice (see Discussion).

143 To implement targeted trimming of the cochlea samples prior to SBEM acquisition,
144 we first acquired X-ray tomographic data from the stained and resin-embedded sample

145 blocks (Fig 1D). This allowed corresponding the cochlear anatomical features observed from
146 tissue block-faces and virtual cross-sections on the tomographic reconstructions (Fig 1E).
147 Based on the standard place-frequency relationship of the mouse cochlea (Muller et al.,
148 2005), we were able to narrow down the best-frequency range of the middle- and basal-
149 turn SBEM volumes (Fig 1F and Appendix Fig S1, 16.2 ± 0.8 kHz and 28.1 ± 1.0 kHz) according
150 to determined anatomical positions. Within these two fixed tonotopic places (16 kHz and 28
151 kHz), we set out to focus on IHC structural comparisons after the synaptopathic exposure
152 (91-dB, 2 h).
153
154 **Enlarged and Multi-ribbons after Acoustic Overexposures.** Using the established image
155 analysis pipeline powered by artificial intelligence (Liu et al., 2022), we volume
156 reconstructed 112 intact IHCs and all 1710 basolateral pole-resided ribbon synapses in the
157 SBEM datasets (Fig 2A and Table 1). As spatial resolution of the SBEM enabled capturing of
158 different ribbon morphologies including multi-ribbons (Fig 2B), we set out to characterize
159 the exposure-related changes of the IHC ribbons. In good agreement with prior LM studies
160 (Fernandez et al., 2015; Grierson et al., 2022; Kujawa and Liberman, 2009; Liberman et al.,
161 2015), a substantial ribbon loss (29.4 %) was observed in the 28 kHz cochlear region
162 following the 91-dB exposure (Fig 2C, 91-dB: 12.0 ± 2.9, n = 46 IHCs) in comparison with the
163 unexposed control group (ctl: 17.0 ± 1.9, n = 33 IHCs, $p < 0.0001$). In the middle (16 kHz)
164 cochlear region, where the 91-dB exposure caused a comparable ABR threshold shift to that
165 of the 28 kHz region, slightly more ribbons per IHC were observed (Fig 2C, 91-dB: 18.1 ± 1.8,
166 n = 33 IHCs, $p = 0.0171$) presumably due to cochlear region-specific difference. These results
167 are consistent to numerous early observations, arguing for a noise-induced ribbon change
168 specifically at high frequency-responsive basal segment of the cochlear BM.

169 Similarly, following the exposures the IHCs tended to have enlarged ribbons in the 28
170 kHz-region (Fig 2D, ctl: 0.0129 ± 0.0004 μm^3, n = 33 IHCs; 91-dB: 0.0184 ± 0.0008 μm^3, n = 46
171 IHCs, $p < 0.0001$), but not in the 16 kHz-region from the same samples (91-dB: 0.0130 ±
172 0.0002 μm^3, n = 33 IHCs, p = 0.7320). The observed volume change was unlikely caused by
173 acute hollowing of synaptic ribbon based on its low occurrence in our datasets (Appendix
174 Fig S2A). Alternatively, additional multi-ribbon AZs might also account for this post-exposure
175 ribbon enlargement, as cumulative ribbon volume was measured on individual AZs,
176 irrespective of single or multiple ribbons (Fig 2B). In fact, we did notice a slight but
177 statistically significant increase in the occurrence of multi-ribbon AZs after the 91-dB
178 exposure (Fig 2E, ctl: 1.70 ± 1.19, n = 33 IHCs; 91-dB: 2.46 ± 1.24, n = 46 IHCs, p = 0.0078),
179 but those IHCs with severe synaptopathy do not necessarily have more multi-ribbon AZs (Fig
180 2E), arguing against the notion that the multi-ribbon AZ is a byproduct of the synaptopathy
181 or a major contributor to the ribbon enlargement. Nevertheless, the cumulative ribbon
182 volume per IHC seemed to be relatively stable in spite of the noise-induced synapse loss
183 (Appendix Fig S2B, ctl: 0.217 ± 0.033 μm^3, n = 33 IHCs; 91-dB: 0.208 ± 0.044 μm^3, n = 46 IHCs,
184 p = 0.3157). Furthermore, an increase in ribbon size heterogeneity was noted in pooled AZs
185 following the synaptopathic exposure (Fig 2F), probably owing to high percentage of the
186 enlarged and multi-ribbons. Besides, the IHC pillar-modiolar gradient of ribbon size was
187 compromised by the exposure (Appendix Fig S2C). Together, these results provide new
188 ultrastructural insights in adaptive plasticity changes of the IHC ribbons.
189
190 **Differential Synaptopathy in the IHCs upon Noise Damage.** It has been recently showed
191 that the staggered mid-cochlea IHCs can be subdivided into two distinct morphological
192 subtypes (Liu et al., 2022; Yin et al., 2014). In both 16 kHz- and 28 kHz-region, we confirmed

193 the copresence of the pillar cell-oriented (type-A) as well as the modiolus-oriented (type-B)
194 subpopulations with opposing ribbon density gradients along the IHC pillar-modiolus axis
195 (Fig 3A). Given that the postsynaptic SGNs with molecular diversity are arranged with
196 distinct spatial preferences (Petitpre et al., 2018; Sherrill et al., 2019; Shrestha et al., 2018;
197 Sun et al., 2018), such alternating IHC basolateral pole positions can be of functional
198 relevance via introducing disproportionated ribbon synapse compositions and thereby
199 differentiate the IHC receptive field of sound intensity (Liu et al., 2022). We then asked
200 whether these two IHC subtypes responded to acoustic insults differently in terms of post-
201 exposure ribbon loss and reorganization.

202 In the 28 kHz-region, the type-A IHCs appeared more alike those located at the
203 cochlear apex, featuring a prominent modiolar-pillar gradient in ribbon size and abundance
204 (Liberman et al., 2011). The post-exposure changes in the type-A IHC ribbons were found
205 exclusively on the modiolar face (Fig 3B, ctl: 10.9 ± 2.2, n = 21 IHCs; 91-dB: 6.9 ± 2.2, n = 30
206 IHCs, $p < 0.0001$), where commonly the ribbon synapses were densely packed. By contrast,
207 their pillar ribbons were more robust to the exposure (Fig 3B, ctl: 6.1 ± 1.6, n = 21 IHCs; 91-
208 dB: 5.6 ± 1.5, n = 30 IHCs, $p = 0.2165$). However, the post-exposure enlargement of the type-
209 A IHC ribbons occurred not only on the modiolar face (Fig 3C, ctl: 0.0142 ± 0.0005 μm^3, n
210 =21 IHCs; 91-dB: 0.0171 ± 0.0008 μm^3, n = 30 IHCs, $p = 0.0088$), but also on the pillar face
211 (ctl: 0.0091 ± 0.0004 μm^3, n = 21 IHCs; 91-dB: 0.0150 ± 0.0008 μm^3, n = 30 IHCs, $p < 0.0001$),
212 which effectively compromised the ribbon size gradient. Besides, the ribbon loss in the 91-
213 dB group resulted in an increased inter-distance of the modiolar ribbons (Fig 3D, ctl: 2.16 ±
214 0.08 µm, n = 21 IHCs; 91-dB: 2.98 ± 0.16 µm, n = 30 IHCs, $p = 0.0002$), diminishing the
215 normal ribbon density gradient along IHC modiolar-pillar axis (ctl: 2.16 ± 0.08 µm versus
216 3.36 ± 0.13 µm, n = 21 IHCs, $p < 0.0001$; 91-dB: 2.98 ± 0.16 µm versus 3.44 ± 0.15 µm, n = 30

217 IHCs, p = 0.0682). These results from the type-A IHCs conform the long-lasting dogma with
218 respect to the modiolar ribbons being more vulnerable to acoustic insults (Liberman et al.,
219 2015).

220 As counterparts, the type-B IHCs appeared to have few but robust modiolar ribbons
221 (Fig 3B, ctl: 3.8 ± 1.2, n = 12 IHCs; 91-dB: 2.3 ± 1.6, n = 16 IHCs, p = 0.0145), while the noise-
222 related changes took place predominantly on the pillar face in terms of reduced ribbon
223 number (Fig 3B, ctl : 13.2 ± 2.1, n = 12 IHCs; 91-dB: 8.7 ± 3.2, n = 16 IHCs, p = 0.0003) and
224 enlarged mean size (Fig 3C, ctl: 0.0134 ± 0.0007 μm^3, n = 12 IHCs; 91-dB: 0.0210 ± 0.0015
225 μm^3, n = 13 IHCs, p = 0.0002). Note that the modiolar preference of ribbons seemed to be
226 maintained in the type-B IHCs following the exposure (Fig 3D, ctl: 3.72 ± 0.38 µm versus 2.41
227 ± 0.08 µm, n = 12 IHCs, p = 0.0048; 91-dB: 3.89 ± 0.37 µm versus 2.80 ± 0.18 µm, n = 11 IHCs,
228 p = 0.0269) in spite of significant ribbon loss and volume change. Together, these results
229 enrich our current view on noise damage in the mid-basal cochlear regions by revealing a
230 set of differences in the post-exposure ribbon organization between two IHC subtypes,
231 which are thought to be equivalently activated upon sensory stimuli.

232

233 **Activity-dependent Remodeling of Synaptic Mitochondrial Network.** In the IHC basolateral
234 compartment, a distance-dependent correlation between the spatial gradient of ribbons
235 and nearby mitochondria was recently reported (Liu et al., 2022). It, however, remains
236 elusive whether the IHC mitochondrial network is adaptively remodeled to the plasticity
237 changes of ribbons. To address this question, the modiolar volume fractions of ribbons and
238 mitochondria were used to compute the correlation coefficients within a domain of growing
239 size from the IHC basolateral pole (Fig 4A and B1). Compared to the unexposed control
240 group, the 91-dB exposure caused an overall reduction in the ribbon-mitochondrion

241 correlation but with similar distance-dependence in the synaptopathic 28 kHz-region
242 (Fig 4B2). Note that the maximum correlations were constantly observed between ribbons
243 and mitochondria within 5 µm from the IHC basal pole (Fig 4B2), implying a strong interplay
244 between ribbons and the adjacent mitochondria. We thereby, nicknamed this anatomical
245 subpopulation as "ribbon-associated mitochondria" or "RAM". Further, we show that the
246 RAM constitute about 15-17 % of total mitochondria in the basal IHC compartment (Fig 4B3,
247 ctl: 17.12 ± 5.70 %, n = 33 IHCs; 91-dB: 15.69 ± 5.72 %, n = 46 IHCs, p = 0.2760). We
248 controlled that such decrease in spatial correlation was caused by redistribution of both
249 ribbons and the RAM following the exposure (Fig 4C and 4D). In addition, we observed a
250 declined fraction of large mitochondria in the pooled RAM following the 91-dB exposure (Fig
251 4E, ctl: 0.0882 ± 0.0008 μm^3, n = 4368; 91-dB: 0.0735 ± 0.0005 μm^3, n = 6065, $p < 0.0001$),
252 presumably owing to activity-dependent mitochondrial fission.
253

254 **Discussion**

255 Mechanosensory hair cells are multi-functionally compartmentalized with specialized
256 organelles, making them attractive model systems for studying the interplay
257 between/among subcellular components including ribbon synapses, synaptic vesicles,
258 mitochondria and membrane cisterns (Chakrabarti et al., 2018; Esterberg et al., 2014;
259 Hashimoto et al., 1990; Kantardzhieva et al., 2013; Lioudyno et al., 2004; Lysakowski and
260 Goldberg, 1997; Spicer et al., 2007; Spicer et al., 1999). By the aid of advanced techniques in
261 serial sectioning, electron microscopy (EM) reconstruction at whole-cell level has become
262 much less labor intensive, contributing to the discoveries of key morphological hallmarks in
263 developing (Michanski et al., 2019; Payne et al., 2021), mature (Bullen et al., 2015; Dow et
264 al., 2015; Hua et al., 2021), aging (Lauer et al., 2012), as well as noise-injured (Bullen et al.,
265 2019) sensory organs.

266 For this study the SBEM is our method of the choice because it is advantageous over
267 other 3D EM as well as LM methods in visualizing large-scale IHC ultrastructure. Sufficient
268 tissue size is critical for determining global orientation of the IHCs by referencing to other
269 cochlear structures, whereas nanometer resolution of the SBEM allows identifying outlines
270 of individual IHC bodies in densely packed regions. These enable comprehensive mapping
271 morphology and cellular distribution of ribbons, especially in the case of noise-damaged
272 IHCs containing orphan and "hollow" ribbons (Liberman et al., 2015; Song et al., 2016).
273 Besides, it is known that cochlear ultrastructure varies along the tonotopic position
274 (Michanski et al., 2019; Payne et al., 2021), but determining precise cochlear locations of
275 the acquired EM volumes in 3D has not yet been established, hampering a reliable inter-
276 sample structural comparison. Recent work has demonstrated x-ray tomography as a
277 powerful tool for morphological study of whole cochleae and its potential to combine with

278 other optical methods (Keppeler et al., 2021; Lu et al., 2021). In the present work, we show
279 the practice of targeting given cochlear tonotopic ranges by using x-ray-tomographic
280 reconstruction to guide sample trimming and sequential SBEM imaging (Appendix Fig S1).

281 Moreover, with ever-growing tissue sizes allowed by improved sample preparation
282 (Genoud et al., 2018; Hua et al., 2021; Hua et al., 2015; Mikula and Denk, 2015) and faster
283 EM acquisition (Hua et al., 2022; Svara et al., 2022; Zheng et al., 2018), image processing has
284 become nowadays a major limitation for high-throughput connectomic and morphomic
285 investigations (Helmstaedter, 2013; Kubota et al., 2018; Varsano and Wolf, 2022). Our
286 recent work has proposed a robust analysis pipeline with full-automated segmentation for
287 IHC outer membranes, ribbon synapses and mitochondria (Liu et al., 2022). Here, we
288 demonstrate that the algorithm is readily applicable for SBEM datasets which were acquired
289 from different animals and cochlear locations (Fig 1A and Table 1). This yields a more than
290 10-fold increase in total number of the reconstructed IHCs as before, boosting
291 ultrastructural profiling of the IHCs under different experimental conditions.

292 In summary, our SBEM quantifications of the IHCs provide an extensive set of
293 observations after acoustic overexposures, including: (1) increased occurrence of large- and
294 multi-ribbon AZs, (2) IHC subtype-specific ribbon changes as well as (3) altered synaptic
295 mitochondrial network. Based on these ultrastructural insights, we gain deeper
296 understanding of the presynaptic concepts underlying activity-dependent ribbon plasticity
297 in the mature IHCs.

298

299 **Synaptopathic and Non-synaptopathic Acoustic Exposures.** Due to the non-linearity of
300 cochlear mechanics, the noise damage including consequent ribbon loss does not directly
301 relate to the magnitude of ABR threshold elevations (see review (Liberman, 2017)). Hence,

302 we calibrated the boundary conditions for synaptopathic (91 dB, 2 h) and non-synaptopathic
303 (85 dB, 2 h) exposures on the juvenile (5-6 weeks) CBA mice (Fig 1B and C) according to the
304 characteristic frequency-profiles of exposure-related ABR threshold shifts on animals at 16
305 weeks of age (Fernandez et al., 2015). Note that our juvenile mice have acquired ribbon loss
306 already after a two-hour exposure at 91 dB, which is considered non-synaptopathic for the
307 mature animal (Fernandez et al., 2015). This result is in line with early study (Kujawa and
308 Liberman, 2006) showing accelerated presbycusis in the young-exposed (4-8 weeks) but not
309 in the old-exposed (≥ 16 weeks) animals to a neuropathic noise (100-dB, 2 h). Taken
310 together, these findings corroborate that the juveniles are more vulnerable to noise-
311 induced hearing loss, both temporary and permanent ones. As permissible noise levels for
312 occupational exposure have been established in adults (Daniell et al., 2006; Davis and
313 Clavier, 2017), preventive actions may be taken with a stricter guideline in school.
314
315 **Ribbon Plasticity and Maintenance in the IHCs.** It has been shown that ribbon size is of
316 functional significance by determining the pool of synaptic vesicles available for fusion and
317 tightly regulated by the presynaptic calcium channels (Frank et al., 2009; Sheets et al., 2012).
318 Although emerging 3D EM techniques have been employed to dissect the morphological
319 maturation of synaptic ribbons, ranging from late embryonic to adult stages (Michanski et
320 al., 2019; Payne et al., 2021), evidences for ribbon maintenance and activity-dependent
321 plasticity are scarce in the mature IHCs. Consistent to prior observations (Liberman et al.,
322 2015), post-exposure ribbons enlargement was observed in the 28 kHz-region (Fig 2D).
323 More importantly, the enlarged ribbons are not associated with "hollowing" cores or
324 obviously fewer tethered vesicles, arguing against a perturbed ribbon function beyond one
325 week after the overexposure. Besides, our quantifications provide emerging evidence for

326 morphological adaptation of the IHC ribbons to sensory experiences via conformational
327 changes. Higher occurrence of multi-ribbon AZs in the synaptopathic group (Fig 2E) is
328 counterintuitive because enhanced synaptic transmission is supposed to make the ribbon
329 synapse more vulnerable due to glutamate-mediated excitotoxicity. Considering that the
330 multi-ribbon AZ is not only retained into adulthood (Hua et al., 2021; Michanski et al., 2019)
331 but also a hallmark of cochlear aging (Stamataki et al., 2006), the functional property of this
332 structural variant remains to be explored. It has been recently proposed (Michanski et al.,
333 2019) that, under the strict constrain of maximum ribbon size in mature IHC, such molecular
334 bypass may allow strengthening of individual synapse to maintain overall neurotransmission
335 level with reduced afferent contacts. In line with this notion, our observations of negatively
336 correlated ribbon number and mean size in an IHC (Hua et al., 2021) may reflect active
337 regulation on the total ribbon volume (Appendix Fig S2B), presumably by cellular
338 homeostasis of the "building block" abundance. Last but not least, enlarged and multi-
339 ribbons lead to an increased synapse heterogeneity following the noise-related
340 synaptopathy (Fig. 2F), suggesting that noise-induced IHC coding deficit is unlikely a simple
341 consequence of the selective loss of large ribbons and may involves maladaptive changes in
342 both pre- and postsynaptic structures.
343
344 **IHC Subtype-specific Ribbon Changes after Noise Exposure.** Our ultrastructural analysis
345 focuses on the 16 kHz- and 28 kHz-regions, where staggered IHCs with alternating
346 basolateral pole positions are prevalent (Yin et al., 2014). They constitute two distinct
347 morphological subpopulations: the abneural-side type-A IHCs having larger and more
348 crowded modiolar ribbons versus the neural-side type-B IHCs with exclusively large ribbons
349 gathering more on the pillar face (Liu et al., 2022). This significant feature implies that two

350 subtypes may differ in their compositions of ribbon synapses, which are tuned to different
351 physiological properties and prefer particular postsynaptic SGN subtypes (Petitpre et al.,
352 2018; Shrestha et al., 2018; Sun et al., 2018). However, it remains largely unexplored
353 whether there is a unifying concept of activity-dependent ribbon plasticity (including the
354 synaptopathy) for both IHC subtypes.

355 It has been shown in the animal models that auditory nerve fibers with low
356 spontaneous rates are more vulnerable than high-spontaneous-rate ones (Furman et al.,
357 2013) and ribbon loss occurs preferentially on the modular IHC face (Liberman et al., 2015).
358 However, this rule may be limited to the basal-most cochlear end, where usually a well-
359 aligned single IHC-row is present. Our results suggest that the worst-hit areas of noise
360 insults are the IHC subregions with high ribbon density, namely modiolar face of the type-A
361 as well as pillar face of the type-B IHC (Fig 3B). In addition, two IHC subtypes undergo
362 distinct post-exposure ribbon reorganization: in the type-A IHCs we observed declined
363 modiolar ribbons, collapsed modiolar-pillar gradients in ribbon size and density; the type-B
364 IHCs simply gain enlarged pillar ribbons including multi-ribbons at the cost of fewer in
365 number, leaving the modular ribbons and the pillar-modiolar gradients largely unaffected
366 (Fig 3C and D). In our view, these IHC subtype-specific differences can neither be readily
367 explained by selective glutamate excitotoxicity on the modiolar (or type *Ic* SGN) nerve
368 terminals (Liberman et al., 2015; Shrestha et al., 2018) nor the protective role of gradient
369 efferent innervations (Boero et al., 2018; Liberman et al., 2014; Maison et al., 2013). In line
370 with this notion, a recent physiology study from CBA mice has revealed noise-induced
371 reduction in both low- and high spontaneous-rate auditory fibers (Suthakar and Liberman,
372 2021). Thus, these evidences argue for a more complex and IHC subtype-specific ribbon
373 plasticity following the classic glutamate-mediated damage on postsynaptic terminals,

374 presumably involving local metabolic stress induced by presynaptic- or mitochondrial-Ca^{2+}
375 influx as well as synaptic vesicle cycle, as recently showed in zebrafish lateral-line hair cells
376 (Lukasz et al., 2022). More importantly, quantification by using a global modiolar-pillar
377 gradient may mask the differences between IHCs in a staggered arrangement, and thereby
378 several prevailing concepts of synaptopathy might not strictly hold true in the functionally
379 more relevant middle cochlea regions.
380
381 **Ribbon-associated Mitochondria in the IHCs.** Sustained neurotransmission at high rate is
382 metabolic demanding for nerve cells. Recent work suggests that the ribbon function is a
383 significant contributor to ATP consumption and reactive oxygen species (ROS) buildup in
384 zebrafish lateral-line hair cells (Lukasz et al., 2022), implying a crucial role of presynaptic
385 mitochondrial network in the maintenance of neurotransmission. In line with this notion,
386 ototoxin susceptibility of hair cells is correlated with mitochondrial activity (Lukasz et al.,
387 2022; Pickett et al., 2018). In the mammalian IHCs, an asymmetric mitochondrial
388 distribution along the radial plane has been previously described (Bullen et al., 2015).
389 Further, our SBEM quantifications of the mid-cochlea (Liu et al., 2022) and the 28-kHz region
390 (this study) corroborate highly correlated spatial gradients of mitochondria and ribbons
391 inside a subcellular domain confined to 4.5 - 5 µm from the basolateral IHC pole (Fig 4B).
392 This finding is significant since it provides a structural cue for defining the putative ribbon-
393 associated mitochondria (RAM). After the synaptopathic exposure, the overall reduction in
394 spatial correlation between mitochondrial and ribbon gradients (Fig 4B) is presumably not
395 only owing to dramatic ribbon reorganization but also caused by activity-dependent
396 mitochondrial remodeling (McQuate et al., 2023). Given that the ribbon size is tightly
397 regulated by the coupled presynaptic influx and mitochondrial uptake of Ca^{2+} (Wong et al.,

398 2019), we attempt to speculate that the altered mitochondrial morphology and basolateral
399 distribution (Fig 4C-E) may hamper the restoration of proper modiolar-pillar ribbon gradient,
400 and thereby contribute to a permanent coding deficit of the IHC. Together, these results
401 argue for a fascinating presynaptic mechanism in hosting the proper ribbon gradient under
402 normal condition, and which may also be involved in the post-insult tuning of
403 neurotransmission in the sensory hair cells.
404

405 **Materials and Methods**

406 **Animals.** In this study, CBA/Ca mice (male, ranging from p28 to p35) were purchased from
407 Shanghai Jihui Experimental Animal Feeding Co., Ltd. (Shanghai, China). Before experiment,
408 animals were raised in the same acoustic environment for maximum seven days.
409 Experiments were conduct at Ear Institute of Shanghai Jiao Tong university School of
410 Medicine and Shanghai Institute of Precision Medicine. All procedures were approved by
411 the Institutional Authority for Laboratory Animal Care of Shanghai Ninth People's Hospital
412 (SH9H-2020-A65-1).

413

414 **Acoustic overexposures.** The acoustic overexposure was carried out in a sound-attenuating
415 chamber (Shanghai Shino Acoustic Equipment Co. Ltd, China). Two acoustic overstimulation
416 protocols were used in this study: an octave-band of noise (8-16 kHz) at 91 or 85 dB for 2
417 hours (Fig 1B). During the exposure, awake animals were kept without restraint in 18 x 18 x
418 10 cm^3 sized cells (1 animal/cell) in a subdivided cage by barbed wires. The cage was placed
419 about directly below the horn of the loudspeaker (X4, HiVi Acoustic, Inc.) connected to a
420 sound card (US-366, TASCAM, Inc.). The octave-band waveform was custom-made (gift from
421 Prof. Bo Zhong, National Institute of Metrology, China) and real-time monitored by Adobe
422 Audition Software. Before each exposure session, the noise was calibrated to the target
423 sound pressure level using an acoustimeter (AWA6228+, Hangzhou Aihua Instruments Co.,
424 Ltd., China) placed in the cage.

425

426 **Auditory Brainstem Responses (ABRs).** ABR measurement were conducted as previously
427 described (Wang et al., 2021; Zhang et al., 2022). In brief, animals were anesthetized, and
428 the body temperature was maintained near 37°C using a regulated heating pad with a

429 thermal probe placed under the abdomen (Homeothermic Monitoring System, Harvard
430 Apparatus, US). Sound stimuli, which was generated by SigGen RP (Tucker-Davis Tech. Inc.,
431 US), were delivered via a speaker (MF1, Tucker-Davis Tech. Inc., US) placed 10 cm away in
432 front of the animal's vertex. ABRs were recorded via three subdermal needle electrodes
433 placed at the animal's vertex (active electrode), left infra-auricular mastoid (reference
434 electrode) and right shoulder region (ground electrode). Signal digitalization and acquisition
435 were done with the software BioSigRZ (Tucker-Davis Tech. Inc., US). The raw signals were
436 amplified (5000x) and bandpass filtered (0.03-5 kHz). The sound level of stimulus started
437 from 90 dB SPL and was decremented in 5 dB steps to ~10 dB below threshold, that was
438 defined as the lowest stimulus needed for evoking visible responses.
439
440 **Sample Preparation.** The *en bloc* EM staining of cochlea was performed following the
441 established protocol (Lu et al., 2021). In brief, after being anesthetized with 2% isoflurane
442 inhalation, animals were decapitated, and temporal bones were dissected from both sides.
443 Under microscope, the cochleae were immediately perfused through the round and oval
444 windows with ice-cold fixative mixture containing 0.08 M cacodylate (pH 7.4, Sigma-Aldrich,
445 US), 2% paraformaldehyde (Sigma-Aldrich, US) and 2.5% glutaraldehyde (Sigma-Aldrich, US).
446 Post-fixation and sequential decalcification were carried out at 4°C by immersing in the
447 same fixative and with addition of 5% EDTA (Sigma-Aldrich, US) for 5 hours each. The
448 decalcified cochleae were then washed twice with 0.15M cacodylate buffer (pH 7.4) for 30
449 min each, and then immersed in 2% OsO_4 (Ted Pella, US), 2.5% ferrocyanide (Sigma-Aldrich,
450 US), and 2% OsO_4 at room temperature for 2, 2, and 1.5 hours, respectively. All staining
451 solutions were buffered with 0.15M cacodylate buffer (pH 7.4). After being washed with
452 0.15M cacodylate buffer and nanopore filtered water for 30 min each, the cochleae were

453 sequentially incubated in 1% freshly made and filtered thiocarbonhydrazide solution
454 (saturated aqueous solution, Sigma-Aldrich, US), 2% OsO_4 aqueous solution and lead
455 aspartate solution (0.03M, pH 5.0, adjusted by KOH) at 50°C for 1, 2 and 2 hours, with
456 immediate washing steps. For embedding, the cochleae were dehydrated through a graded
457 acetone-water mixture (50%, 75%, 90% acetone at 4°C for 30 min each) into pure acetone (3
458 times at room temperature for 30 min each). Then the dehydrated cochleae were infiltrated
459 with 1:1 mixture of acetone and Spurr resin monomer (4.1g ERL 4221, 0.95g DER 736, 5.9g
460 NSA and 1% DMAE; Sigma-Aldrich, US) at room temperature for 6 hours on a rotator,
461 followed by 1:2 mixture of acetone and resin monomer at room temperature for overnight
462 on a rotator. Infiltrated cochleae were then incubated in pure resin for 8-12 hours before
463 being placed in embedding molds (Polyscience, Germany) and incubated in a pre-warmed
464 oven at 70°C for at least 72 hours.
465
466 **Correlative X-ray Microscopy (XRM) and Serial Block-face Electron Microscopy (SBEM).** For
467 high-resolution XRM imaging of the cochlea, excess resin around cochlea was carefully
468 removed using a trimmer (TRIM2, Leica, Germany) equipped with a diamond knife head
469 (#227172, Anton Meyer & Co. Ltd). Cochlea samples were mounted upright along the
470 conical center axis on an aluminum metal rivet (3VMRS12, Gatan, UK) and scanned with an
471 XRM (Xradia 520 Versa, Carl Zeiss, Germany) at a pixel size of < 4.7 µm, source voltage 60 kV,
472 power 5 W and exposure time per radiograph 1 sec. Cochlear 3D reconstructions based on
473 acquired XRM datasets were visualized and further analyzed in 3D image processing
474 software (AMIRA, Thermo Scientific, US). Whole extent of the basilar membrane was
475 annotated with marked segments of interest using published mouse cochlear place-
476 frequency map as reference (Muller et al., 2005). After having trimmed the cochleae

477 coronally to the targeted location, we imaged (30 × 30 nm^2, 60 × 60 μm^2 per image) the
478 block-face of each sample using a SEM (Gemini300, Carl Zeiss, Germany) for *post hoc*
479 confirmation of the frequency range of the SBEM volumes.

480 The samples were remounted with the previously SEM-scanned block-face on top
481 and further trimmed down to a block size of about 800 × 800 x 500 μm^3 (xyz). Serial sections
482 were imaged using a field-emission SEM (Gemini300, Carl Zeiss) equipped with an in-
483 chamber ultramicrotome (3ViewXP, Gatan) and back-scattered electron detector (Onpoint,
484 Gatan). In total, six SBEM datasets were analyzed in this study (Fig 1A), two (M1 and M2) of
485 unexposed cochleae, as well as four (M3-4, two from each animal) of noise exposed
486 cochleae. Imaging parameters were as follows: incident electron beam energy, 2 keV; pixel
487 dwell time, 1.5-2.0 µs; pixel size, 12 nm; cutting thickness 50 nm; focal charge compensation,
488 100%; vacuum chamber pressure, ~2.8×10^{-3} mbar. Consecutively acquired slices were
489 aligned offline using cross-correlation function in MATLB (MathWorks, US) and cubed for
490 volume tracing in webKNOSSOS (Boergens et al., 2017; Hua et al., 2021).

491

492 **Reconstruction of IHC, Mitochondrion and Ribbon Synapse.** Using the previously trained
493 3D u-net models (Liu et al., 2022), the in-plane probability maps of IHCs and mitochondria
494 were generated by running the networks with a blocking-scheme. Distance-transform-
495 watershed algorithm was applied to each thresholded probability map to produce over-
496 segmented super-pixels for IHCs and mitochondria. To achieve volume reconstruction, we
497 used 3D connection algorithm to connect the 2D super-pixels and output the reconstructed
498 3D objects. From all the datasets, 112 IHCs were volume reconstructed. Automatic
499 detection and segmentation were carried out for all 115,115 associated mitochondria
500 residing in those IHCs (n=79) of the 28-kHz cochlear region (M1-4). Manual proof-reading

501 and correction were done in webKNOSSOS (Boergens et al., 2017) on the auto-
502 segmentation results of total 1710 ribbon synapses. The coronal plane of each IHC was
503 determined by two lines and its center point. The first line was parallel to one IHC row
504 which was computed by fitting a line with IHC centers on it. Another line was the principal
505 axis of each IHC computed by principal component analysis (PCA). Each IHC cell body was
506 then divided into pillar and modiolar hemispheres based on the coronal plane and with
507 individual ribbon synapses assigned objectively to either hemisphere.
508
509 **Statistical Analysis.** All data analysis and statistical tests were carried out using self-written
510 scripts and built-in functions in MATLAB (release 2021a) and the Statistics Toolbox
511 (MathWorks, Inc., US). The comparisons between groups were done using two-sample t-test
512 (*ttest2*) for Fig 1C, 2C-E, S2A-B, 3B-D, 4B3 and paired t-test (*ttest1*) for Fig S2C. The
513 distribution comparisons between groups were done using two-sample Kolmogorov-
514 Smirnov tests (*kstest2*) for Figure 2F, 4B3, 4E. The significance level of statistical tests was
515 denoted as n.s. for $p > 0.05$, * for $p < 0.05$, ** for $p < 0.01$, *** for $p < 0.001$ and **** for $p <$
516 0.0001.

517 **References**
518
519 Boergens, K.M., Berning, M., Bocklisch, T., Braunlein, D., Drawitsch, F., Frohnhofen, J.,
520 Herold, T., Otto, P., Rzepka, N., Werkmeister, T.*, et al.* (2017). webKnossos: efficient online
521 3D data annotation for connectomics. Nat Methods *14*, 691-694.
522 Boero, L.E., Castagna, V.C., Di Guilmi, M.N., Goutman, J.D., Elgoyhen, A.B., and Gomez-
523 Casati, M.E. (2018). Enhancement of the Medial Olivocochlear System Prevents Hidden
524 Hearing Loss. J Neurosci *38*, 7440-7451.
525 Bullen, A., Anderson, L., Bakay, W., and Forge, A. (2019). Localized disorganization of the
526 cochlear inner hair cell synaptic region after noise exposure. Biol Open *8*.
527 Bullen, A., West, T., Moores, C., Ashmore, J., Fleck, R.A., MacLellan-Gibson, K., and Forge, A.
528 (2015). Association of intracellular and synaptic organization in cochlear inner hair cells
529 revealed by 3D electron microscopy. J Cell Sci *128*, 2529-2540.
530 Chakrabarti, R., Michanski, S., and Wichmann, C. (2018). Vesicle sub-pool organization at
531 inner hair cell ribbon synapses. EMBO Rep *19*.
532 Daniell, W.E., Swan, S.S., McDaniel, M.M., Camp, J.E., Cohen, M.A., and Stebbins, J.G. (2006).
533 Noise exposure and hearing loss prevention programmes after 20 years of regulations in the
534 United States. Occup Environ Med *63*, 343-351.
535 Davis, R.R., and Clavier, O. (2017). Impulsive noise: A brief review. Hear Res *349*, 34-36.
536 Dow, E., Siletti, K., and Hudspeth, A.J. (2015). Cellular projections from sensory hair cells
537 form polarity-specific scaffolds during synaptogenesis. Genes Dev *29*, 1087-1094.
538 Esterberg, R., Hailey, D.W., Rubel, E.W., and Raible, D.W. (2014). ER-mitochondrial calcium
539 flow underlies vulnerability of mechanosensory hair cells to damage. J Neurosci *34*, 9703-
540 9719.
541 Fernandez, K.A., Jeffers, P.W., Lall, K., Liberman, M.C., and Kujawa, S.G. (2015). Aging after
542 noise exposure: acceleration of cochlear synaptopathy in "recovered" ears. J Neurosci *35*,
543 7509-7520.
544 Fettiplace, R. (2017). Hair Cell Transduction, Tuning, and Synaptic Transmission in the
545 Mammalian Cochlea. Compr Physiol *7*, 1197-1227.
546 Frank, T., Khimich, D., Neef, A., and Moser, T. (2009). Mechanisms contributing to synaptic
547 Ca2+ signals and their heterogeneity in hair cells. Proc Natl Acad Sci U S A *106*, 4483-4488.
548 Frank, T., Rutherford, M.A., Strenzke, N., Neef, A., Pangrsic, T., Khimich, D., Fejtova, A.,
549 Gundelfinger, E.D., Liberman, M.C., Harke, B.*, et al.* (2010). Bassoon and the synaptic ribbon
550 organize Ca(2)+ channels and vesicles to add release sites and promote refilling. Neuron *68*,
551 724-738.
552 Furman, A.C., Kujawa, S.G., and Liberman, M.C. (2013). Noise-induced cochlear neuropathy
553 is selective for fibers with low spontaneous rates. J Neurophysiol *110*, 577-586.
554 Genoud, C., Titze, B., Graff-Meyer, A., and Friedrich, R.W. (2018). Fast Homogeneous En Bloc
555 Staining of Large Tissue Samples for Volume Electron Microscopy. Front Neuroanat *12*, 76.
556 Grierson, K.E., Hickman, T.T., and Liberman, M.C. (2022). Dopaminergic and cholinergic
557 innervation in the mouse cochlea after noise-induced or age-related synaptopathy. Hear Res
558 *422*, 108533.
559 Hashimoto, S., Kimura, R.S., and Takasaka, T. (1990). Computer-aided three-dimensional
560 reconstruction of the inner hair cells and their nerve endings in the guinea pig cochlea. Acta
561 Otolaryngol *109*, 228-234.
562 Heil, P., and Peterson, A.J. (2015). Basic response properties of auditory nerve fibers: a
563 review. Cell Tissue Res *361*, 129-158.

564 Helmstaedter, M. (2013). Cellular-resolution connectomics: challenges of dense neural
565 circuit reconstruction. Nat Methods *10*, 501-507.
566 Hickman, T.T., Hashimoto, K., Liberman, L.D., and Liberman, M.C. (2020). Synaptic migration
567 and reorganization after noise exposure suggests regeneration in a mature mammalian
568 cochlea. Sci Rep *10*, 19945.
569 Hua, Y., Ding, X., Wang, H., Wang, F., Lu, Y., Neef, J., Gao, Y., Moser, T., and Wu, H. (2021).
570 Electron Microscopic Reconstruction of Neural Circuitry in the Cochlea. Cell Rep *34*, 108551.
571 Hua, Y., Laserstein, P., and Helmstaedter, M. (2015). Large-volume en-bloc staining for
572 electron microscopy-based connectomics. Nat Commun *6*, 7923.
573 Hua, Y., Loomba, S., Pawlak, V., Voit, K.M., Laserstein, P., Boergens, K.M., Wallace, D.J., Kerr,
574 J.N.D., and Helmstaedter, M. (2022). Connectomic analysis of thalamus-driven disinhibition
575 in cortical layer 4. Cell Rep *41*, 111476.
576 Huet, A., Batrel, C., Wang, J., Desmadryl, G., Nouvian, R., Puel, J.L., and Bourien, J. (2019).
577 Sound Coding in the Auditory Nerve: From Single Fiber Activity to Cochlear Mass Potentials
578 in Gerbils. Neuroscience *407*, 83-92.
579 Joselevitch, C., and Zenisek, D. (2020). Direct Observation of Vesicle Transport on the
580 Synaptic Ribbon Provides Evidence That Vesicles Are Mobilized and Prepared Rapidly for
581 Release. J Neurosci *40*, 7390-7404.
582 Kantardzhieva, A., Liberman, M.C., and Sewell, W.F. (2013). Quantitative analysis of ribbons,
583 vesicles, and cisterns at the cat inner hair cell synapse: correlations with spontaneous rate. J
584 Comp Neurol *521*, 3260-3271.
585 Keppeler, D., Kampshoff, C.A., Thirumalai, A., Duque-Afonso, C.J., Schaeper, J.J., Quilitz, T.,
586 Topperwien, M., Vogl, C., Hessler, R., Meyer, A.*, et al.* (2021). Multiscale photonic imaging of
587 the native and implanted cochlea. Proc Natl Acad Sci U S A *118*.
588 Kubota, Y., Sohn, J., and Kawaguchi, Y. (2018). Large Volume Electron Microscopy and
589 Neural Microcircuit Analysis. Front Neural Circuits *12*, 98.
590 Kujawa, S.G., and Liberman, M.C. (2006). Acceleration of age-related hearing loss by early
591 noise exposure: evidence of a misspent youth. J Neurosci *26*, 2115-2123.
592 Kujawa, S.G., and Liberman, M.C. (2009). Adding insult to injury: cochlear nerve
593 degeneration after "temporary" noise-induced hearing loss. J Neurosci *29*, 14077-14085.
594 Kujawa, S.G., and Liberman, M.C. (2015). Synaptopathy in the noise-exposed and aging
595 cochlea: Primary neural degeneration in acquired sensorineural hearing loss. Hear Res *330*,
596 191-199.
597 Lauer, A.M., Fuchs, P.A., Ryugo, D.K., and Francis, H.W. (2012). Efferent synapses return to
598 inner hair cells in the aging cochlea. Neurobiol Aging *33*, 2892-2902.
599 Liberman, L.D., Suzuki, J., and Liberman, M.C. (2015). Dynamics of cochlear synaptopathy
600 after acoustic overexposure. J Assoc Res Otolaryngol *16*, 205-219.
601 Liberman, L.D., Wang, H., and Liberman, M.C. (2011). Opposing gradients of ribbon size and
602 AMPA receptor expression underlie sensitivity differences among cochlear-nerve/hair-cell
603 synapses. J Neurosci *31*, 801-808.
604 Liberman, M.C. (2017). Noise-induced and age-related hearing loss: new perspectives and
605 potential therapies. F1000Res *6*, 927.
606 Liberman, M.C., Dodds, L.W., and Pierce, S. (1990). Afferent and efferent innervation of the
607 cat cochlea: quantitative analysis with light and electron microscopy. J Comp Neurol *301*,
608 443-460.
609 Liberman, M.C., Liberman, L.D., and Maison, S.F. (2014). Efferent feedback slows cochlear
610 aging. J Neurosci *34*, 4599-4607.

611 Lioudyno, M., Hiel, H., Kong, J.H., Katz, E., Waldman, E., Parameshwaran-Iyer, S., Glowatzki,
612 E., and Fuchs, P.A. (2004). A "synaptoplasmic cistern" mediates rapid inhibition of cochlear
613 hair cells. J Neurosci *24*, 11160-11164.
614 Liu, J., Wang, S., Lu, Y., Wang, H., Wang, F., Qiu, M., Xie, Q., Han, H., and Hua, Y. (2022).
615 Aligned Organization of Synapses and Mitochondria in Auditory Hair Cells. Neurosci Bull *38*,
616 235-248.
617 Lu, Y., Wang, F., Wang, H., Bastians, P., and Hua, Y. (2021). Large-scale 3D imaging of mouse
618 cochlea using serial block-face scanning electron microscopy. STAR Protoc *2*, 100515.
619 Lukasz, D., Beirl, A., and Kindt, K. (2022). Chronic neurotransmission increases the
620 susceptibility of lateral-line hair cells to ototoxic insults. Elife *11*.
621 Lysakowski, A., and Goldberg, J.M. (1997). A regional ultrastructural analysis of the cellular
622 and synaptic architecture in the chinchilla cristae ampullares. J Comp Neurol *389*, 419-443.
623 Maison, S.F., Usubuchi, H., and Liberman, M.C. (2013). Efferent feedback minimizes cochlear
624 neuropathy from moderate noise exposure. J Neurosci *33*, 5542-5552.
625 McQuate, A., Knecht, S., and Raible, D.W. (2023). Activity regulates a cell type-specific
626 mitochondrial phenotype in zebrafish lateral line hair cells. Elife *12*.
627 Meyer, A.C., Frank, T., Khimich, D., Hoch, G., Riedel, D., Chapochnikov, N.M., Yarin, Y.M.,
628 Harke, B., Hell, S.W., Egner, A.*, et al.* (2009). Tuning of synapse number, structure and
629 function in the cochlea. Nat Neurosci *12*, 444-453.
630 Michanski, S., Smaluch, K., Steyer, A.M., Chakrabarti, R., Setz, C., Oestreicher, D., Fischer, C.,
631 Mobius, W., Moser, T., Vogl, C.*, et al.* (2019). Mapping developmental maturation of inner
632 hair cell ribbon synapses in the apical mouse cochlea. Proc Natl Acad Sci U S A *116*, 6415-
633 6424.
634 Mikula, S., and Denk, W. (2015). High-resolution whole-brain staining for electron
635 microscopic circuit reconstruction. Nat Methods *12*, 541-546.
636 Moser, T., Grabner, C.P., and Schmitz, F. (2020). Sensory Processing at Ribbon Synapses in
637 the Retina and the Cochlea. Physiol Rev *100*, 103-144.
638 Muller, M., von Hunerbein, K., Hoidis, S., and Smolders, J.W. (2005). A physiological place-
639 frequency map of the cochlea in the CBA/J mouse. Hear Res *202*, 63-73.
640 Pangrsic, T., Singer, J.H., and Koschak, A. (2018). Voltage-Gated Calcium Channels: Key
641 Players in Sensory Coding in the Retina and the Inner Ear. Physiol Rev *98*, 2063-2096.
642 Payne, S.A., Joens, M.S., Chung, H., Skigen, N., Frank, A., Gattani, S., Vaughn, K., Schwed, A.,
643 Nester, M., Bhattacharyya, A.*, et al.* (2021). Maturation of Heterogeneity in Afferent
644 Synapse Ultrastructure in the Mouse Cochlea. Front Synaptic Neurosci *13*, 678575.
645 Petitpre, C., Wu, H., Sharma, A., Tokarska, A., Fontanet, P., Wang, Y., Helmbacher, F., Yackle,
646 K., Silberberg, G., Hadjab, S.*, et al.* (2018). Neuronal heterogeneity and stereotyped
647 connectivity in the auditory afferent system. Nat Commun *9*, 3691.
648 Pickett, S.B., Thomas, E.D., Sebe, J.Y., Linbo, T., Esterberg, R., Hailey, D.W., and Raible, D.W.
649 (2018). Cumulative mitochondrial activity correlates with ototoxin susceptibility in zebrafish
650 mechanosensory hair cells. Elife *7*.
651 Safieddine, S., El-Amraoui, A., and Petit, C. (2012). The auditory hair cell ribbon synapse:
652 from assembly to function. Annu Rev Neurosci *35*, 509-528.
653 Sergeyenko, Y., Lall, K., Liberman, M.C., and Kujawa, S.G. (2013). Age-related cochlear
654 synaptopathy: an early-onset contributor to auditory functional decline. J Neurosci *33*,
655 13686-13694.

656 Sheets, L., Kindt, K.S., and Nicolson, T. (2012). Presynaptic CaV1.3 channels regulate synaptic
657 ribbon size and are required for synaptic maintenance in sensory hair cells. J Neurosci *32*,
658 17273-17286.
659 Sherrill, H.E., Jean, P., Driver, E.C., Sanders, T.R., Fitzgerald, T.S., Moser, T., and Kelley, M.W.
660 (2019). Pou4f1 Defines a Subgroup of Type I Spiral Ganglion Neurons and Is Necessary for
661 Normal Inner Hair Cell Presynaptic Ca(2+) Signaling. J Neurosci *39*, 5284-5298.
662 Shi, L., Chang, Y., Li, X., Aiken, S.J., Liu, L., and Wang, J. (2016). Coding Deficits in Noise-
663 Induced Hidden Hearing Loss May Stem from Incomplete Repair of Ribbon Synapses in the
664 Cochlea. Front Neurosci *10*, 231.
665 Shrestha, B.R., Chia, C., Wu, L., Kujawa, S.G., Liberman, M.C., and Goodrich, L.V. (2018).
666 Sensory Neuron Diversity in the Inner Ear Is Shaped by Activity. Cell *174*, 1229-1246 e1217.
667 Song, Q., Shen, P., Li, X., Shi, L., Liu, L., Wang, J., Yu, Z., Stephen, K., Aiken, S., Yin, S.*, et al.*
668 (2016). Coding deficits in hidden hearing loss induced by noise: the nature and impacts. Sci
669 Rep *6*, 25200.
670 Spicer, S.S., Qu, C., Smythe, N., and Schulte, B.A. (2007). Mitochondria-activated cisternae
671 generate the cell specific vesicles in auditory hair cells. Hear Res *233*, 40-45.
672 Spicer, S.S., Thomopoulos, G.N., and Schulte, B.A. (1999). Novel membranous structures in
673 apical and basal compartments of inner hair cells. J Comp Neurol *409*, 424-437.
674 Stamataki, S., Francis, H.W., Lehar, M., May, B.J., and Ryugo, D.K. (2006). Synaptic
675 alterations at inner hair cells precede spiral ganglion cell loss in aging C57BL/6J mice. Hear
676 Res *221*, 104-118.
677 Sun, S., Babola, T., Pregernig, G., So, K.S., Nguyen, M., Su, S.M., Palermo, A.T., Bergles, D.E.,
678 Burns, J.C., and Muller, U. (2018). Hair Cell Mechanotransduction Regulates Spontaneous
679 Activity and Spiral Ganglion Subtype Specification in the Auditory System. Cell *174*, 1247-
680 1263 e1215.
681 Suthakar, K., and Liberman, M.C. (2021). Auditory-nerve responses in mice with noise-
682 induced cochlear synaptopathy. J Neurophysiol *126*, 2027-2038.
683 Svara, F., Forster, D., Kubo, F., Januszewski, M., Dal Maschio, M., Schubert, P.J., Kornfeld, J.,
684 Wanner, A.A., Laurell, E., Denk, W.*, et al.* (2022). Automated synapse-level reconstruction of
685 neural circuits in the larval zebrafish brain. Nat Methods.
686 Vaithianathan, T., Henry, D., Akmentin, W., and Matthews, G. (2016). Nanoscale dynamics
687 of synaptic vesicle trafficking and fusion at the presynaptic active zone. Elife *5*.
688 Varsano, N., and Wolf, S.G. (2022). Electron microscopy of cellular ultrastructure in three
689 dimensions. Curr Opin Struct Biol *76*, 102444.
690 Wang, H., Li, B., Lu, Y., Han, K., Sheng, H., Zhou, J., Qi, Y., Wang, X., Huang, Z., Song, L.*, et al.*
691 (2021). Real-time threshold determination of auditory brainstem responses by cross-
692 correlation analysis. iScience *24*, 103285.
693 Wong, A.B., Rutherford, M.A., Gabrielaitis, M., Pangrsic, T., Gottfert, F., Frank, T., Michanski,
694 S., Hell, S., Wolf, F., Wichmann, C.*, et al.* (2014). Developmental refinement of hair cell
695 synapses tightens the coupling of Ca2+ influx to exocytosis. EMBO J *33*, 247-264.
696 Wong, H.C., Zhang, Q., Beirl, A.J., Petralia, R.S., Wang, Y.X., and Kindt, K. (2019). Synaptic
697 mitochondria regulate hair-cell synapse size and function. Elife *8*.
698 Wu, P.Z., Liberman, L.D., Bennett, K., de Gruttola, V., O'Malley, J.T., and Liberman, M.C.
699 (2019). Primary Neural Degeneration in the Human Cochlea: Evidence for Hidden Hearing
700 Loss in the Aging Ear. Neuroscience *407*, 8-20.

701 Yin, Y., Liberman, L.D., Maison, S.F., and Liberman, M.C. (2014). Olivocochlear innervation
702 maintains the normal modiolar-pillar and habenular-cuticular gradients in cochlear synaptic
703 morphology. J Assoc Res Otolaryngol *15*, 571-583.
704 Zhang, Y., Lin, G., Wang, Y., Xue, N., Lin, X., Du, T., Xiong, W., and Song, L. (2022). Prestin
705 derived OHC surface area reduction underlies age-related rescaling of frequency place
706 coding. Hear Res *423*, 108406.
707 Zheng, Z., Lauritzen, J.S., Perlman, E., Robinson, C.G., Nichols, M., Milkie, D., Torrens, O.,
708 Price, J., Fisher, C.B., Sharifi, N.*, et al.* (2018). A Complete Electron Microscopy Volume of
709 the Brain of Adult Drosophila melanogaster. Cell *174*, 730-743 e722.
710
711

Tables

Table 1. SBEM datasets from four CBA mice

	M1	M2	M3	M3	M4	M4
Sex & Age	Male, from p42 to p35					
Noise exposure	no	no	8-16 kHz, 91dB		8-16 kHz, 91dB	
Cochlear frequency (kHz)	27.8*	28.3*	15.6	26.9	16.7	29.4
Resolution (nm^3)	12 × 12 × 50	12 × 12 × 50	12 × 12 × 50	12 × 12 × 50	12 × 12 × 50	12 × 12 × 50
Volume (μm^3)	148 × 295× 154	124 × 302 × 128	177 × 268 × 109	125 × 251× 146	200 × 234 × 122	128× 360 × 139
# IHCs	15	18	16	20	17	26
# ribbons / IHC	**17.9 ± 2.0**	**16.3 ± 1.6**	**18.6 ± 2.0**	**12.5 ± 2.0**	**17.7 ± 1.5**	**11.6 ± 3.4**

*Represents the estimated value.
Data are represented as mean ± SD.

717 **Figures**

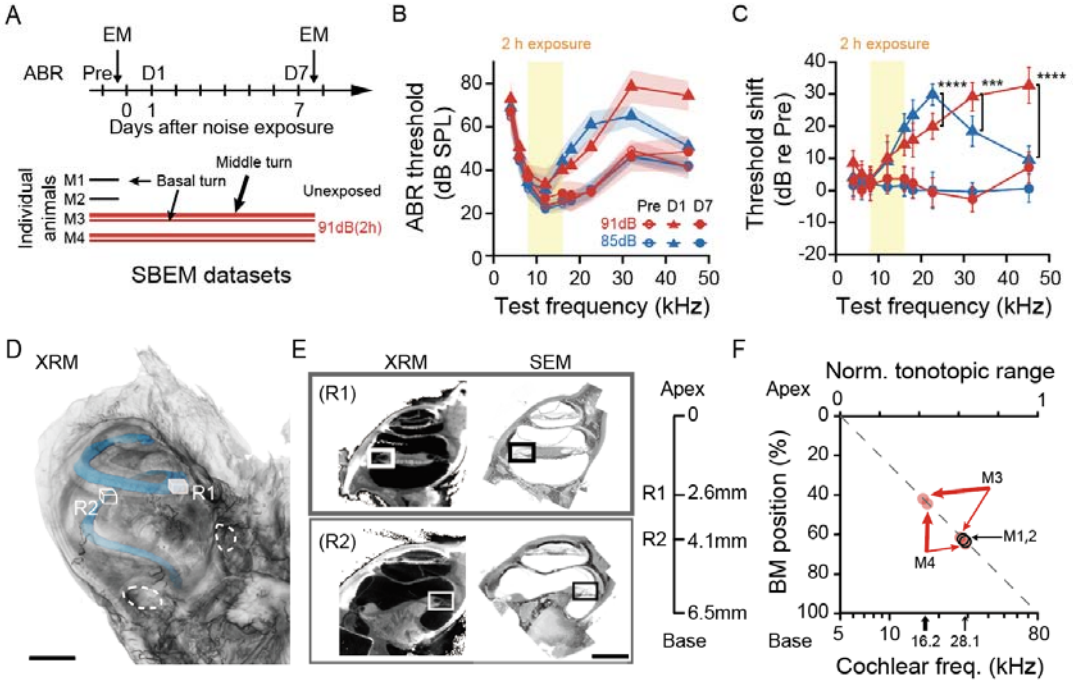

718

719 **Figure 1. SBEM imaging of the noise exposed cochleae.**

720 (A) Experimental design (top): hearing thresholds were determined by auditory brainstem
721 responses (ABRs) before (Pre), on the day-1 (D1) and the day-7 (D7) after the noise
722 exposure. Cochlea samples were collected either from the unexposed animals or on the D7
723 from the exposed ones. SBEM datasets (bottom): six EM volumes were acquired from four
724 male CBA mice (M1 to M4, p35-42) at the middle (thick line) or/and basal (thin line)
725 cochlear turns. Two were taken from the unexposed animals (M1/2, black) and the others
726 were from the animals receiving a 2-hour pure-tone (8-16 kHz) exposure at 91 dB (red,
727 M3/4).

728 (B) Both 85 dB (blue, n = 10 animals) and 91 dB (red, n = 7 animals) exposures produced a
729 transient elevation in hearing thresholds on the D1 (triangles) which was fully recovered on

730 the D7 (filled circles) in comparison with the baseline values before exposure (Pre, empty
731 circles).
732 (C) Relative ABR threshold shifts computed from (B). Different threshold shifts on the D1
733 after the 85- (blue) and the 91-dB (red) exposures at the best-frequencies of 22.6 kHz (30.00
734 ± 1.05 dB vs. 20.00 ± 0.99 dB, two-sample t-test, $p < 0.0001$), 32 kHz (18.50 ± 1.50 dB vs.
735 29.29 ± 1.09 dB, $p = 0.0003$) and 45.2 kHz (9.50 ± 1.38 dB vs. 32.86 ± 1.38 dB, $p < 0.0001$).
736 Data are presented as group means ± SEM.
737 (D) Volume rendering of reconstructed X-ray micrographs (XRM) taken from the cochlea
738 sample. Two SBEM datasets are located in the middle-turn (R1) as well as the basal-turn (R2)
739 on the cochlear basilar membrane (BM, pseudo-blue). Round window (below) and oval
740 window (right) are indicated by dashed circles. Scale bar represents 500 µm.
741 (E) Matched anatomical features between the XRM tomographic virtual sections (left) and
742 the EM images of sample block-faces (right) for targeted sample trimming and *post-hoc*
743 determination of the SBEM imaged locations (small boxes) in the middle (thick grey box)
744 and basal (thin grey box) cochlear turn. Scale bar represents 500 µm.
745 (F) Relative BM locations determined for individual SBEM volumes (the control group: black
746 circles; the 91-dB group: red dots), which were used to infer the best-frequencies of the
747 imaged IHCs based on a normalized tonotopic range from 5 to 80 kHz and yielded 16.2 ± 0.8
748 kHz and 28.1 ± 1.0 kHz for the middle (thick arrows) and basal (thin arrows) turn datasets,
749 respectively.
750

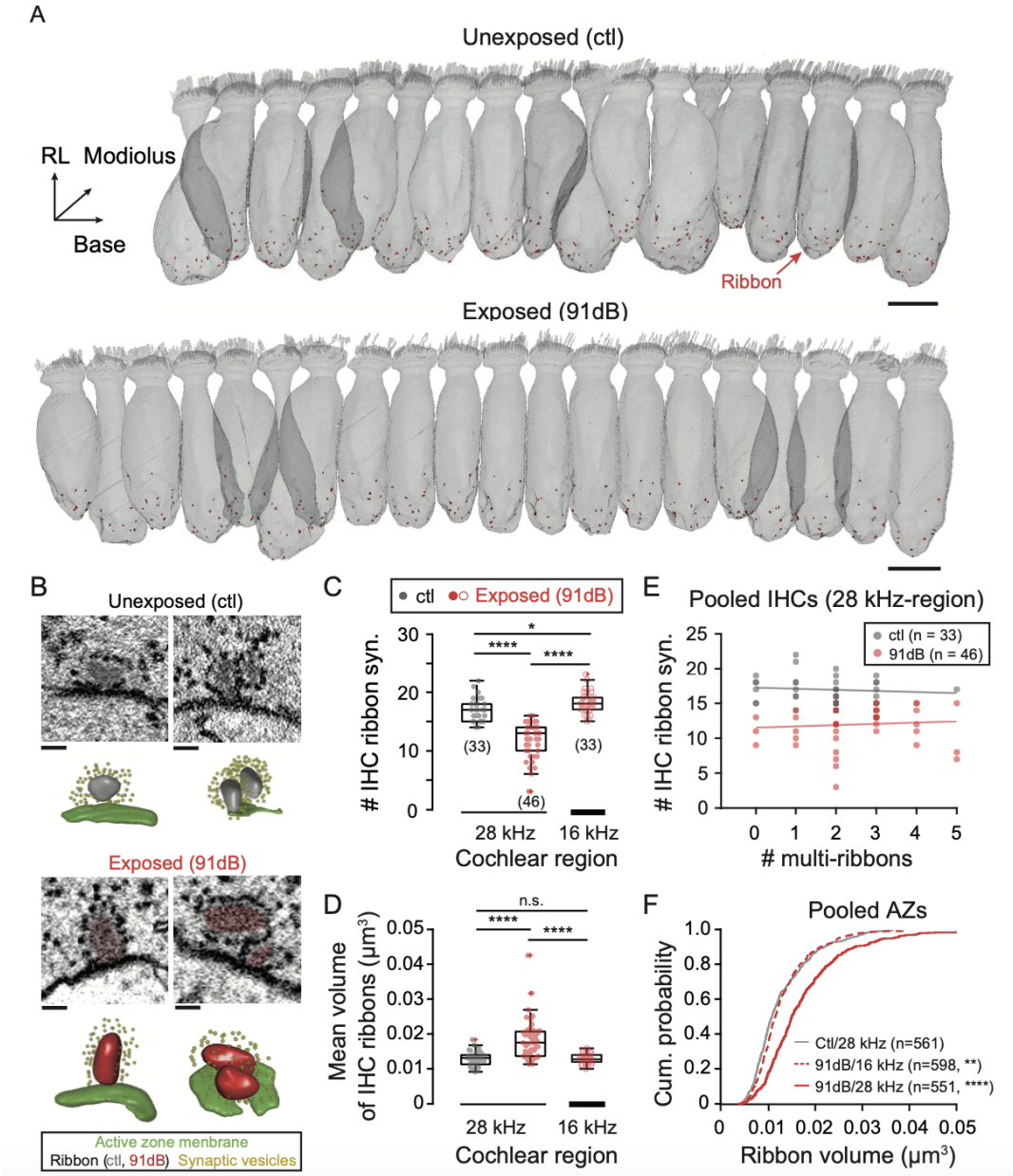

Figure 2. 3D morphological quantifications of IHC ribbons.

(A) For illustration, volume rendering of 18 reconstructed IHCs (grey) and 20 reconstructed IHCs (grey) from the control (ctl) and the exposed group (91dB) respectively. Red dots at the IHC basolateral surface represent the synaptic ribbons. Scale bar represents 20 µm.

(B) Example electron micrographs of single-ribbon (left) and multi-ribbon (right) AZs from the control (ctl) and the exposed group (91dB). For illustration, reconstructed ribbon

758 synapses including AZ membrane (green), ribbon (grey or red) and SVs (yellow) are showed
759 in 3D. Scale bars represent 0.2 μm.
760 (C) Comparisons of IHC ribbon numbers among the unexposed group (ctl, grey dots) and the
761 91-dB group (91dB, red dots). In the 28-kHz region: 17.0 ± 1.9, n = 33 IHCs (ctl); 12.0 ± 2.9, n
762 = 46 IHCs (91dB). Two-sample t-test, $p < 0.0001$ (ctl vs. 91dB). In the 16-kHz region: 18.1 ±
763 1.8, n = 33 IHCs (91dB). Two-sample t-test, $p = 0.0171$ (ctl vs. 91dB) and $p < 0.0001$ (91dB:
764 28 kHz vs. 16 kHz).
765 (D) Comparisons of mean ribbon volume per IHC among the exposed and unexposed groups.
766 In the 28-kHz region: 0.0129 ± 0.0004 μm^3, n = 33 IHCs (ctl); 0.0184 ± 0.0008 μm^3, n = 46
767 IHCs (91dB). Two-sample t-test, $p < 0.0001$ (ctl vs. 91dB). In the 16-kHz region: 0.0130 ±
768 0.0002 μm^3, n = 33 IHCs (91dB). Two-sample t-test, $p = 0.7320$ (ctl vs. 91dB) and $p < 0.0001$
769 (91dB: 28 kHz vs. 16 kHz).
770 (E) Scatterplot of number of ribbon synapses and multi-ribbons per IHC. In the 28-kHz region:
771 1.70 ± 1.19, n = 33 IHCs (ctl); 2.46 ± 1.24, n = 46 IHCs (91dB). Two-sample t-test, $p = 0.0078$
772 (ctl vs. 91dB).
773 (F) Cumulative probability distribution of ribbon size from pooled AZs in the 16-kHz and 28-
774 kHz region, respectively. The median and mean volumes of ribbons are 0.0108 μm^3 and
775 0.0128 ± 0.0064 μm^3 (ctl, n = 561 AZs), 0.0115 μm^3 and 0.0130 ± 0.0058 μm^3 (91dB: 16 kHz,
776 n = 598 AZs), 0.0151 μm^3 and 0.0174 ± 0.0092 μm^3 (91dB: 28 kHz, n = 551 AZs), respectively.
777 Two-sample Kolmogorov-Smirnov test, $p = 0.0043$ (ctl vs. 91dB: 16 kHz) and $p < 0.0001$ (ctl
778 vs. 91dB: 28 kHz). Data in 2C-D are presented as mean ± SEM. Data in 2F is presented as
779 mean ± SD.

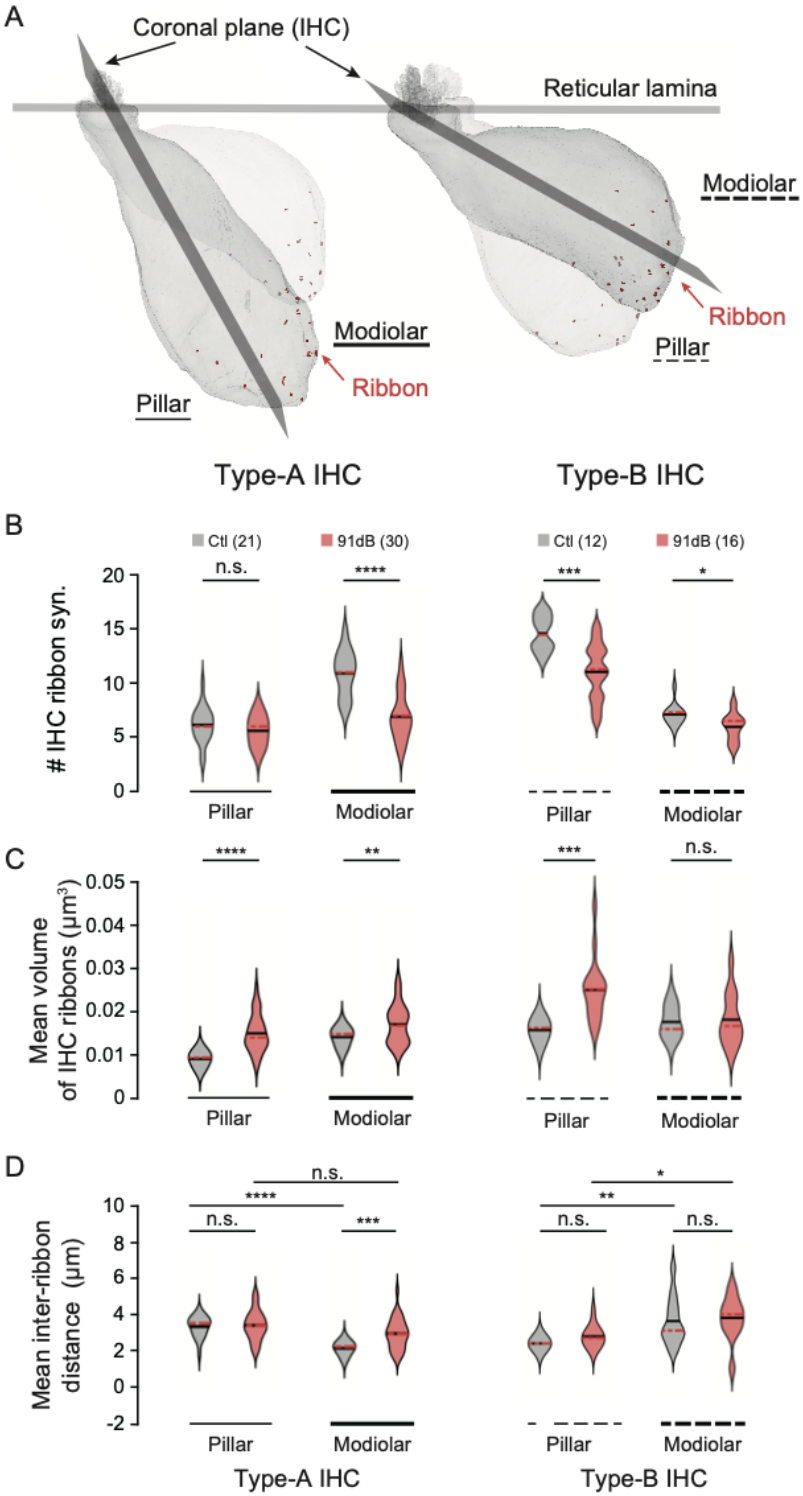

Figure 3. IHC subtype-specific, post-exposure ribbon reorganization.

(A) Example pairs of type-A (left – dark grey, right – light grey) and type-B IHCs (left – light grey, right – dark grey) are showed in sagittal view. They differ to each other by

784 characteristic tilting of the coronal plane, which divides the cell body into pillar (solid and
785 dashed thin lines) and modiolar hemispheres (solid and dashed thick lines).
786 (B) Left: comparisons of ribbon numbers in the 28-kHz region among the type-A IHCs (solid
787 lines) of different groups (grey: the control group; red: the 91-dB group). On the modiolar
788 IHC face, the ribbon numbers are 10.9 ± 2.2 (ctl, n = 21 IHCs) and 6.9 ± 2.2 (91dB, n = 30
789 IHCs). Two-sample t-test, $p < 0.0001$ (ctl vs. 91dB). Whereas there is no significant difference
790 among the pillar ribbons (ctl: 6.1 ± 1.6; 91dB: 5.6 ± 1.5). Two-sample t-test, $p = 0.2165$ (ctl vs.
791 91dB). Right: same comparison for the type-B IHCs (dashed lines). The modiolar ribbons are
792 few in number but comparable with different groups (ctl: 3.8 ± 1.2, n = 12 IHCs; 91dB: 2.3 ±
793 1.6, n = 16 IHCs, $p = 0.0145$), whereas the exposures impact on the abundance of pillar
794 ribbons significantly (ctl: 13.2 ± 2.1; 91dB: 8.7 ± 3.2). Two-sample t-test, $p = 0.0003$ (ctl vs.
795 91dB). Black and red lines represent the mean and the median, respectively.
796 (C) Comparisons of average ribbon volume in the IHCs. As for the type-A IHCs (solid lines),
797 significant ribbon enlargements occur in both modiolar and pillar IHC faces of the 91-dB
798 group (red). Modiolar ribbons: 0.0142 ± 0.0005 μm^3 (ctl, n = 21 IHCs) and 0.0171 ± 0.0008
799 μm^3 (91dB, n = 30 IHCs). Two-sample t-test, $p = 0.0088$ (ctl vs. 91dB). Pillar ribbons: 0.0091 ±
800 0.0004 μm^3 (ctl, n = 21 IHCs) and 0.0150 ± 0.0008 μm^3 (91dB, n = 30 IHCs). Two-sample t-
801 test, $p < 0.0001$ (ctl vs. 91dB). As for the type-B IHCs (dashed lines), ribbon size changes are
802 evident only on the pillar IHC face. Modiolar ribbons: 0.0153 ± 0.0011 μm^3 (ctl, n = 12 IHCs)
803 and 0.0158 ± 0.0017 μm^3 (91dB, n = 13 IHCs). Two-sample t-test, $p = 0.7963$ (ctl vs. 91dB).
804 Pillar ribbons: 0.0134 ± 0.0007 μm^3 (ctl, n = 12 IHCs) and 0.0210 ± 0.0015 μm^3 (91dB, n = 13
805 IHCs). Two-sample t-test, $p = 0.0002$ (ctl vs. 91dB).
806 (D) Comparisons of inter-ribbon distances as a measure of local ribbon density. The
807 modiolar face of type-A IHCs (thick solid line): 2.16 ± 0.08 µm (ctl, n = 21 IHCs) and 2.98 ±

808 0.16 µm (91dB, n = 30 IHCs). Two-sample t-test, p = 0.0002 (ctl vs. 91dB). The pillar face of
809 type-A IHCs (thin solid line): 3.36 ± 0.13 µm (ctl, n = 21 IHCs) and 3.44 ± 0.15 µm (91dB, n =
810 30 IHCs). Two-sample t-test, p = 0.7322 (ctl vs. 91dB). The modiolar face of type-B IHCs
811 (thick dashed line): 3.72 ± 0.38 µm (ctl, n = 12 IHCs) and 3.89 ± 0.37 µm (91dB, n = 11 IHCs).
812 Two-sample t-test, p = 0.7416 (ctl vs. 91dB). The pillar face of type-B IHCs (thin dashed line):
813 2.41 ± 0.08 µm (ctl, n = 12 IHCs) and 2.80 ± 0.18 µm (91dB, n = 11 IHCs). Two-sample t-test,
814 p = 0.0553 (ctl vs. 91dB). All data are presented as mean ± SEM.
815

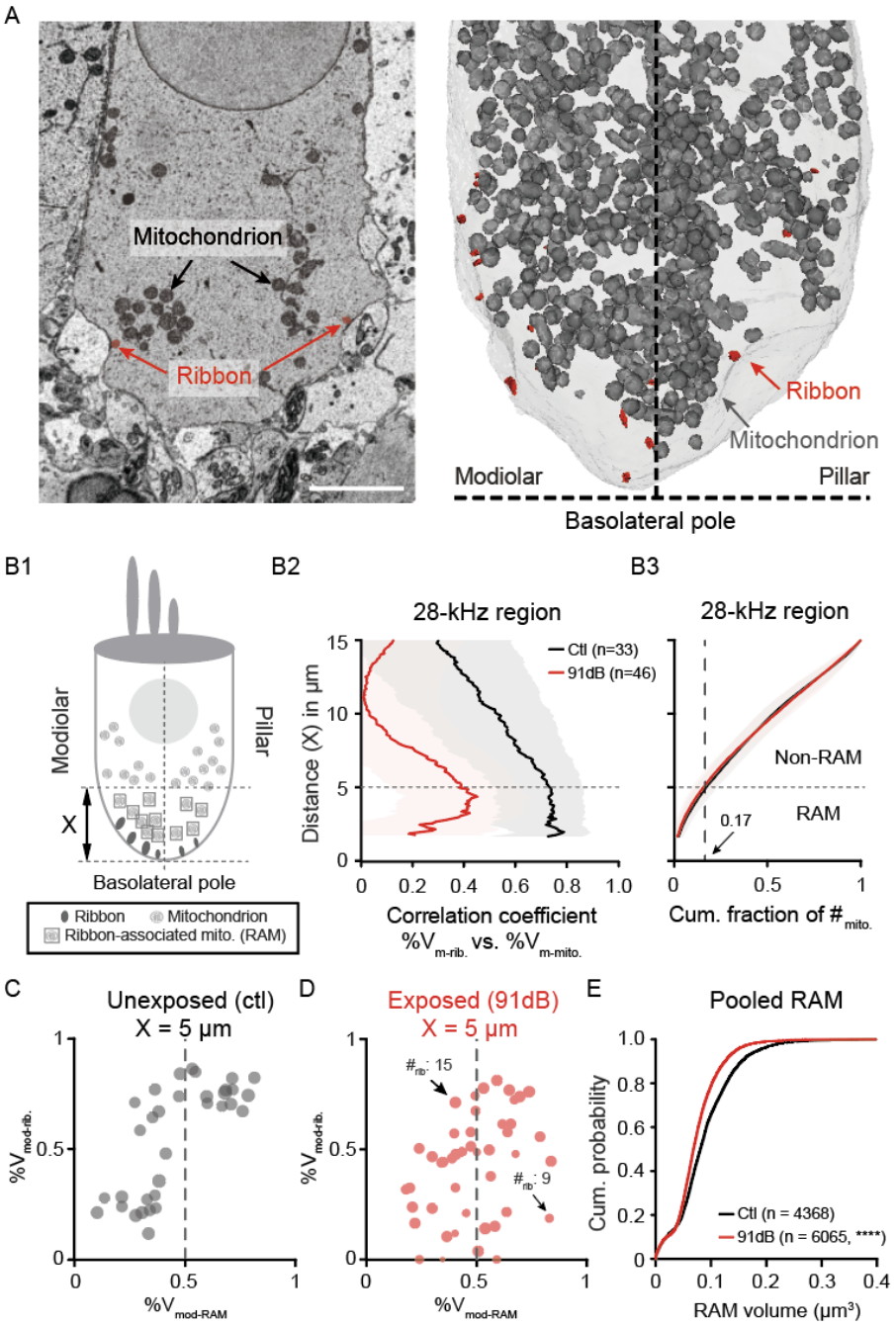

Figure 4. Activity-dependent remodeling of ribbon-associated mitochondria.

(A) Left: electron micrograph of a representative IHC (basal compartment), in which synaptic ribbons (red arrow) and mitochondria (grey arrow) are visible. Scale bar represents 5µm. Right: 3D rendering of volume reconstructed ribbons (red) and mitochondria (grey).

821 (B1) Schematic depicting of ribbon and mitochondrial distribution at the IHC basal
822 compartment. With increase in the distance from the basolateral IHC pole (X), more
823 mitochondria are included in the correlation analysis with the ribbon gradient. Note that the
824 type-A and type B IHCs have opposing ribbon gradients.
825 (B2) Correlation coefficients computed between modiolar fraction of the ribbons ($\%V_{m\text{-}rib.}$)
826 and that of the mitochondria ($\%V_{m\text{-}mito.}$) within a varying distance from the IHC pole. The
827 peak correlations between ribbons and mitochondria are reached at X = 5 µm (dashed line)
828 in the control (black) and 91-dB groups (red).
829 (B3) Cumulative fraction of the mitochondrion number ($\#_{mito.}$) along the IHC middle axis
830 reveals similar radial profiles of mitochondrial distribution in the control (black) and the 91-
831 dB group (red). Number fractions of the ribbon-associated mitochondria (RAM, within 5 µm
832 from the IHC pole) are 0.1712 ± 0.0570 (ctl, n = 33 IHCs) and 0.1569 ± 0.0572 (91dB, n = 46
833 IHCs). Two-sample t-test, p = 0.2760 (ctl vs. 91dB). Two-sample Kolmogorov-Smirnov test, p
834 = 0.2400 (ctl vs. 91dB).
835 (C and D) Scatterplot of volume fraction of the modiolar ribbons with that of the RAM in the
836 unexposed (C, ctl, grey dots) and the exposed group (D, 91dB, red dots). The size of each dot
837 represents the number of ribbons per IHC.
838 (E) Cumulative fractions of pooled RAM volumes. The median and mean RAM volumes are
839 0.0808 μm^3 and 0.0882 ± 0.0542 μm^3 (ctl, n = 4368), 0.0686 μm^3 and 0.0735 ± 0.0425 μm^3
840 (91dB, n = 6065), respectively. Two-sample Kolmogorov-Smirnov test, $p < 0.0001$. (ctl vs.
841 91dB). Data in 4B are presented as mean ± SD. Black and red lines represent the mean and
842 the median, respectively.